How to cite: Angew. Chem. Int. Ed. 2024, e202401344
doi.org/10.1002/anie.202401344

Photocatalysis

Directed Electron Delivery from a Pb-Free Halide Perovskite to a Co(II) Molecular Catalyst Boosts CO_2 Photoreduction Coupled with Water Oxidation

Jin-Shuang Zhao[+], Yan-Fei Mu[+], Li-Yuan Wu, Zhi-Mei Luo, Lucia Velasco, Maxime Sauvan, Dooshaye Moonshiram, Jia-Wei Wang, Min Zhang,* and Tong-Bu Lu**

Abstract: The development of high-performance photocatalytic systems for CO_2 reduction is appealing to address energy and environmental issues, while it is challenging to avoid using toxic metals and organic sacrificial reagents. We here immobilize a family of cobalt phthalocyanine catalysts on Pb-free halide perovskite $Cs_2AgBiBr_6$ nanosheets with delicate control on the anchors of the cobalt catalysts. Among them, the molecular hybrid photocatalyst assembled by carboxyl anchors achieves the optimal performance with an electron consumption rate of $300 \pm 13\ \mu mol\ g^{-1} h^{-1}$ for visible-light-driven CO_2-to-CO conversion coupled with water oxidation to O_2, over 8 times of the unmodified $Cs_2AgBiBr_6$ ($36 \pm 8\ \mu mol\ g^{-1} h^{-1}$), also far surpassing the documented systems ($< 150\ \mu mol\ g^{-1} h^{-1}$). Besides the improved intrinsic activity, electrochemical, computational, ex-/in situ X-ray photoelectron and X-ray absorption spectroscopic results indicate that the electrons photogenerated at the Bi atoms of $Cs_2AgBiBr_6$ can be directionally transferred to the cobalt catalyst via the carboxyl anchors which strongly bind to the Bi atoms, substantially facilitating the interfacial electron transfer kinetics and thereby the photocatalysis.

Introduction

The sunlight-driven CO_2 reduction is a sustainable way to resolve the problem of the green house effect with water as the electron source to produce fuels and high-value chemical feedstocks.[1–2] However, the involvement of multiple electron/proton transfer processes in CO_2 reduction and the diverse product distribution along with competitive H_2 evolution both demand the rational design of efficient and selective photocatalytic systems.[3] It will be more attractive to fabricate the catalytic systems with only earth-abundant elements in order to avoid the high expense and scarcity from noble-based metals.[4–5] Semiconducting metal halide perovskite (MHP) continues to attract attention in constructing high-performance photocatalytic systems for CO_2 reduction with their earth-abundant nature and broad visible-light absorption.[6–12] They are also highly advantageous in their strong oxidizing forces which can drive the oxidation of water as the electron source instead of organic sacrificial reagents,[13–16] realizing more sustainable artificial photosynthetic systems. Nonetheless, the performances of the reported MHP-based systems for CO_2 photoreduction are partially hampered by the absence of efficient active sites.[17] Without efficient active sites to bind and activate CO_2 molecule, the reduction of inert CO_2 molecules will be lethargic, resulting in slower electron consumption and thus severe charge recombination, ultimately leading to much-compromised performance.[18]

In this context, the immobilization of molecular catalysts is promising to solve the above problem by acting as the efficient CO_2-reduction active sites on the MHP, which should enhance the electron utilization and thus relieve the charge recombination. Molecular catalysts based on metal complexes are of high efficiency with their well-defined structures and facile mechanistic studies.[19–23] But their performances are limited by moderate stability, poor conductivity and aggregation tendencies,[24] which can also be circumvented by their rational dispersion on suitable functional surfaces. Previous studies have tried to immobilize a Re-bipyridine,[10] a Ni-terpyridine[11] or a Fe-porphyrin[16] catalyst on $CsPbBr_3$ nanocrystals, or a dinuclear Co-cryptate catalyst on Pb-free $Cs_3Sb_2Br_9$ hollow nanospheres,[9] most of which utilized different organic sacrificial reagents, to achieve good performances in CO_2 photoreduction. Nonetheless, these instances have exhibited restricted promise in sustainable applications owing to their use of toxic (Pb) metals and/or organic sacrificial reagents. Moreover, the delicate control on the anchors of molecular catalysts is still underexplored among the above precedents, partially leading to their unsatisfying performances. Indeed, the anchors

[*] J.-S. Zhao,[+] Y.-F. Mu,[+] L.-Y. Wu, M. Zhang, T.-B. Lu
MOE International Joint Laboratory of Materials Microstructure, Institute for New Energy Materials and Low Carbon Technologies, School of Materials Science and Engineering, Tianjin University of Technology, 300384 Tianjin, China
E-mail: zm2016@email.tjut.edu.cn
lutongbu@tjut.edu.cn
Z.-M. Luo, J.-W. Wang
School of Chemical Engineering and Technology, Sun Yat-sen University, 519082 Zhuhai, China
E-mail: wangjw89@mail.sysu.edu.cn
L. Velasco, M. Sauvan, D. Moonshiram
Instituto de Ciencia de Materiales de Madrid (ICMM-CSIC), Sor Juana Inés de la Cruz, 3, 28049 Madrid, Spain
[+] Equal contribution

of the molecular catalysts play key roles in affecting the catalytic activity of the catalysts themselves by imposing substantial electronic effects,[25–26] as well as tuning the electronic interactions with the MHP surface.[27] Beyond these merits, we expect that the ideal anchors can also pinpoint the photogenerated-electron-localized atoms on the semiconducting surface, which should serve as the directed electron-transfer channels to further facilitate the interfacial electron delivery.

As the proof of concept, we present a family of Pb-free-MHP molecular hybrid photocatalysts consisting of $Cs_2AgBiBr_6$ (**CABB**) nanosheets and a family of cobalt molecular catalysts, including pristine (**CoPc**), cobalt tetraamino phthalocyanine (**CoTAPc**) and cobalt phthalocyanine tetracarboxylic acid (**CoTCPc**), for CO_2 photoreduction to CO with water as the electron source. Among the three Co-based photocatalysts, **CoTCPc@CABB** molecular hybrid photocatalyst exhibits the highest CO generate rate of 150 ± 6 μmol g^{-1} h^{-1} coupled with stoichiometric formation of O_2 from water oxidation, more than 8 times of the one with pristine **CABB**, which is also consistent with the record-high electron consumption rate of 300 ± 13 μmol g^{-1} h^{-1} among the reported MHP photocatalysts for CO_2 reduction coupled with water oxidation. As anticipated, systematic experimental and computational studies have revealed that the carboxyl anchors of **CoTCPc** play important roles in connecting to the Bi atoms which provide the photoexcited electrons, building a directional electron-delivery pathway between **CoTCPc** and **CABB** and greatly contributing to the remarkable photocatalytic performance.

Results and Discussion

Synthesis and Characterization of CABB and CoPc-Derived Catalysts

The Pb-free **CABB** nanosheets were synthesized as orange powders by a temperature-varied procedure (Figure 1A; see Supporting Information for details). The powder X-ray diffraction (PXRD; Figure S1) pattern of the as-prepared **CABB** sample matches well with the simulation pattern of the cubic double MHP crystal phase with the space group $Fm\bar{3}m$.[28–29] Transmission electron microscopy (TEM; Figure 1B) image of **CABB** reveals rectangular nanosheets with an average edge length of ca. 120 nm. High-resolution TEM (HRTEM; Figure 1C) image exhibits the well-defined interplanar distance of 0.28 nm, corresponding to the (400) plane, which is consistent with the relatively intense signal from the (400) plane in its PXRD pattern (Figure S1). The elemental mapping of **CABB** nanosheets (Figure S2) demonstrates that Cs, Ag, Bi and Br elements are uniformly dispersed in the nanosheets. The atomic force microscopy (AFM; Figure S3) results display the around 8 nm thickness of the **CABB** nanosheets. Subsequently, the band gap properties of **CABB** were examined by UV/Vis diffuse reflectance spectroscopy (UV/Vis-DRS; Figure S4) and UV photoelectron spectroscopy (UPS; Figure S5), indicating a conduction band (CB) potential of −0.90 V (vs. NHE at pH 7.0) and a valence band (VB) value of 1.35 V, which are sufficiently strong to drive CO_2 reduction to CO (−0.52 V) and water oxidation to O_2 (0.82 V),[30] respectively.

On the other hand, the redox properties of cobalt catalysts (structures shown in Figure 1A) were investigated by cyclic voltammetry (CV) in DMF solutions (Figure S6) with summarized electrochemical data in Table S1. We note that these electrochemical results only serve as comparisons in the redox and catalytic abilities of the cobalt catalysts, rather than the indications of thermodynamic matching with the components in photocatalytic CO_2 reduction, because

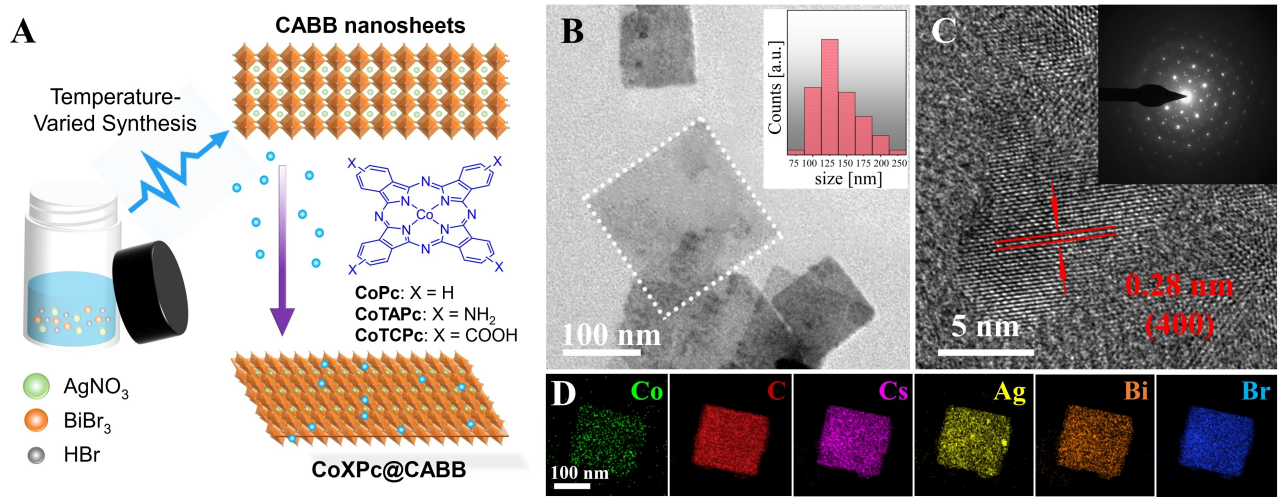

Figure 1. (A) Synthetic Scheme of **CABB** and **CABB**-based molecular hybrid photocatalysts. (B) TEM and (C) HRTEM images of **CABB** nanosheets. (D) EDS mapping of **CoTCPc@CABB**.

they were operated under different conditions. Under Ar, their CV curves all exhibit three reduction waves, consistent with initial metal-centered $Co^{II/I}$ reduction, and two subsequent ligand-centered reduction events.[31] The first $Co^{II/I}$ redox couples in the CV curves of **CoTAPc**, **CoPc** and **CoTCPc** display an increasingly positive trend from −0.45 to −0.34 then to −0.16 V (vs. NHE unless otherwise stated), in good agreement with the increasing electron-withdrawing abilities of the functional groups. Upon the introduction of CO_2, enhanced currents were observed at the third redox couples of all cobalt catalysts, suggesting the catalytic CO_2 reduction. The onset potentials of the catalytic currents[32] (Figure S6 and Table S1; −1.22, −1.10 and −0.92 V) also exhibit an increasingly positive order along with the increasing electron-withdrawing groups on the corresponding cobalt phthalocyanines, demonstrating that the carboxyl anchors endows the lowest overpotential for **CoTCPc** in catalytic CO_2 reduction, which will favor the photocatalysis driven by the same semiconductor (**CABB**).

Synthesis and Characterization of CABB-Based Molecular Hybrids

The immobilization of **CoPc** derivatives on the **CABB** surfaces was operated by simply mixing the catalyst solutions and **CABB** nanosheets, followed by drying, giving rise to **CoPc@CABB**, **CoTCPc@CABB** and **CoTAPc@CABB** samples (see Supporting Information for details). UV/Vis-DRS results of these hybrid materials demonstrate the characteristic Q band absorption of cobalt phthalocyanines, respectively (Figure S4). Inductively coupled plasma mass spectrometry (ICP-MS) was used to quantify the cobalt contents in these samples, displaying similar loadings (3–4 w %; Table S2), consistent with the results of energy-dispersive X-ray spectroscopy (EDS) analyses with atomic percentage (Figure S7 and Table S3). PXRD measurements confirm that the crystal phase and crystallinity of **CABB** samples were maintained with the immobilization of cobalt catalysts (Figure S8). Their EDS mapping results show the homogeneous distribution of cobalt elements on the nanosheets (Figures 1D, S9 and S10) with retention of the nanosheet-like morphology, which further indicates the successful incorporation of these cobalt catalysts in **CABB**.

More importantly, the chemical compositions and electronic interactions between different **CoPc** derivatives and **CABB** were examined by high-resolution X-ray photoelectron spectroscopy (XPS; Figures 2A, 2B, S11–S13). It can be seen that **CABB** contains Ag, Bi and Br elements, while additional signals corresponding to the Co element are observed for **CoPc@CABB**, **CoTCPc@CABB** and **CoTAPc@CABB** samples, consistent with the anchorage of the cobalt catalysts on **CABB**. Moreover, the binding

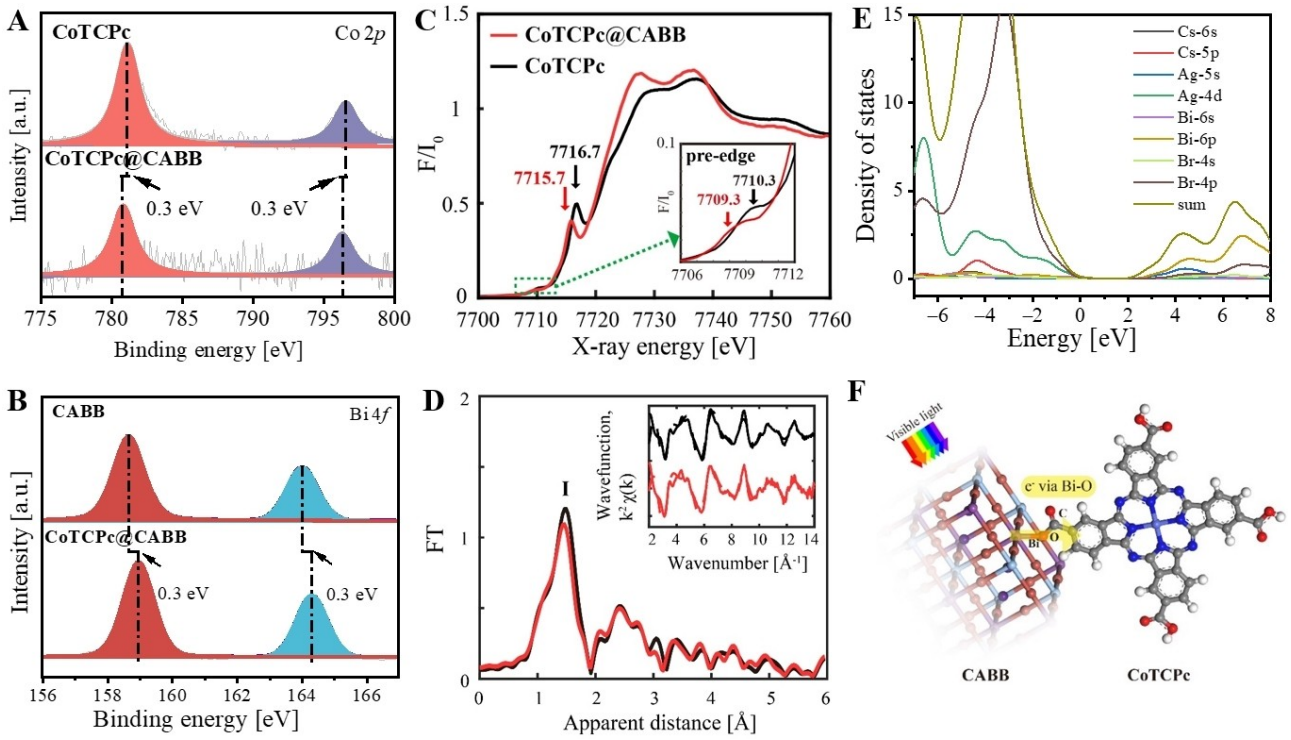

Figure 2. (A) Co 2p XPS spectra of **CoTCPc** (up) and **CoTCPc@CABB** (down). (B) Bi 4*f* XPS spectra of **CABB** (up) and **CoTCPc@CABB** (down). (C) Normalized Co K-edge XANES spectra recorded at 20 K of **CoTCPc** (black) together with **CoTCPc@CABB** (red). Inset shows the magnified view of the pre-edge regions. (D) Fourier transforms of k^2-weighted Co EXAFS of **CoTCPc** (black) and **CoTCPc@CABB** (red). Inset shows the back Fourier transformed experimental (solid) and fitted (dashed) $k_2[\chi(k)]$ of the Co complexes. Experimental spectra were calculated for *k* values of 2–14 $Å^{-1}$. (E) Calculated partial density of states (PDOS) for **CABB**. (F) Expected binding model of **CoTCPc@CABB**.

energies of these elements exhibit varying shifts upon the immobilizations of different cobalt catalysts, indicating their different electronic interactions with **CABB**. It can be noticed that these shift variations (Table S4) are in increasing order of **CoPc** < **CoTAPc** < **CoTCPc**, consistent with the trend of their binding strengths on the **CABB** surface. These observations further manifest that the amino and carboxyl anchors are both effective in reinforcing the binding, in addition to their non-covalent interactions, between molecular catalysts and **CABB**. For **CoTAPc**, the amino anchors tend to interact with Br atoms on **CABB** via weak hydrogen bonding.[33–34] For **CoTCPc**, the carboxyl anchors should be more able to bind with Bi atoms through the strong coordination bond for its good affinity to O donors.[35] Besides the C–O–Bi coordination via the carboxyl groups, non-covalent π–π and van der Waals interactions should coexist at the phthalocyanine-material interfaces.[24,36] Additionally, the negative shifts in Co binding energies of **CoTCPc** upon immobilization on **CABB** can be tentatively attributed to the deprotonation of the carboxyl groups when coordinated to Bi, rather than the coordination from the surface Br atoms to the Co centers. The latter assumption is less possible owing to the conversely positive shifts in Co binding energies in the cases of **CoPc** and **CoTAPc** (Table S4), where the assumed Co–Br coordination should also take place.

To further confirm the coordination environment and the electronic variation of Co center of **CoTCPc** in the **CoTCPc@CABB** hybrid material, X-ray absorption near edge structure (XANES) and extended X-ray absorption fine structure (EXAFS) measurements of **CoTCPc** and **CoTCPc@CABB** were carried out. In Figure 2C, the Co K-edge XANES of **CoTCPc** displays a prominent peak corresponding to the 1s→4p_z transition at 7716.7 eV whereas that deposited on the **CABB** surface displays the 1s→4p_z peak at 7715.7 eV as previously observed for four-coordinated Co complexes.[37–39] The XANES spectra of **CoTCPc** and its **CABB**-anchored form both display pre-edge peaks at 7709.3 and 7710.3 eV, corresponding to 1s to 3d quadrupole transitions and dipole excitations of their core electrons into the valence 3d states and ligand p orbitals,[40–42] respectively (Figure 2C inset). Interestingly, the XANES spectra of **CoTCPc** before and after anchorage illustrate additional changes in the rising edge features within 7710–7730 eV, consistent with the variations in the coordination spheres and local symmetry. Importantly, **CoTCPc@CABB** illustrates an increased electron density vs. the bare **CoTCPc** as indicated by a negative edge energy shift of 0.48 eV from 7721.04 to 7720.56 eV between their XANES spectra. This notable shift is consistent with the above XPS observations, further confirming the strong interactions between **CoTCPc** and **CABB** in the molecular hybrid. Additionally, the EXAFS fits for the extraction of the actual bond lengths of both complexes are further shown in Figure 2D inset and Table S5. Both analyses of the EXAFS spectrum of **CoTCPc** and **CoTCPc@CABB** reveal four Co–N distances of 1.93 Å, in close agreement with the density functional theory (DFT) optimized coordinates (Co–N = 1.93 Å; Appendix), demonstrating the molecular nature of the catalyst upon immobilization on the **CABB** surface. Overall, the above XPS, XAS and computational results clearly demonstrate the substantial electronic interactions via carboxyl anchors between **CoTCPc** and **CABB**, which should facilitate the interfacial electron transfer and therefore improve the photocatalytic performance.

The advantage of such a binding mode between the carboxyl anchors and Bi sites was further verified by the computational studies on the partial density of state (PDOS) of **CABB** using the Perdue–Burke–Ernzerhof (PBE) of the generalized gradient approximation function (see Supporting Information and Figure S14 for details). As shown in Figure 2E, the VB maximum of **CABB** is primarily contributed by a filled Br 4p state, while the CB minimum is mainly composed of empty antibonding Ag 5s and Bi 6p states, indicating that the VB-to-CB transition is largely from filled Br 3p/4p states to antibonding Ag 5s and dominantly Bi 6p states. This implies that the photogenerated electrons are primarily accumulated at mainly the Bi sites. Therefore, in the **CoTCPc@CABB** hybrid material, the good matching between **CoTCPc** and **CABB** by binding at the Bi sites through the carboxyl anchors should achieve directional, rapid electron transfer from the photoexcited **CABB** to **CoTCPc**. As indicated by the XPS results (Figure 2A and 2B), the notable positive shifts in the Bi binding energies of **CABB** as well as the negative ones in Co binding energies of **CoTCPc** within **CoTCPc@CABB** both suggest the effective electron extraction from **CABB** to **CoTCPc** at the ground state, presumably via the C–O–Bi linkages (Figure 2F).

The above speculations were further confirmed by the in situ irradiated XPS (ISI-XPS) experiments, as depicted in Figures 3A, 3B, S15–S18 with their binding energy data summarized in Table S6. Specifically, the Bi 4*f* and Ag 3*d* binding energy in **CABB** both shifted to the lower energy direction (ΔBE = −0.1~−0.2 eV) after illumination (Figures S15A and S16 A), demonstrating the accumulation of photogenerated electrons at the Bi/Ag sites, consistent with the result of DOS calculation in Figure 2E. In sharp contrast, with the immobilization of each cobalt catalyst, the binding energy values of Bi/Ag upon illumination presented positive shifts instead (ΔBE = +0.1~+0.3 eV), which can be attributed to the extraction of photogenerated electrons from Bi/Ag to the cobalt centers. Among the molecular hybrid photocatalysts, **CoTCPc@CABB** displays the most substantial differences compared to the bare **CABB** in terms of the light-induced shifts (ΔBE) in Bi/Ag binding energy values, as exemplified by the maximum difference of 0.5 eV for the Bi 4*f* binding energy (ΔBE = −0.2 eV for **CABB** vs. +0.3 eV for **CoTCPc@CABB**; Figures 3A and S15), which corresponds to the most favored electron transfer via the carboxyl linkers. Meanwhile, the Co binding energy values of these cobalt molecular hybrid photocatalysts all show negative shifts under illumination (Figures 3B and S18), in agreement with the $Co^{II/I}$ reduction powered by the electron injection into the cobalt catalysts from the excited **CABB**, where, more importantly, the most marked negative shift of Co 2*p* binding energy (ΔBE = −0.3 eV for Co $2p_{3/2}$) was observed on **CoTCPc@CABB**. Consequently, the substan-

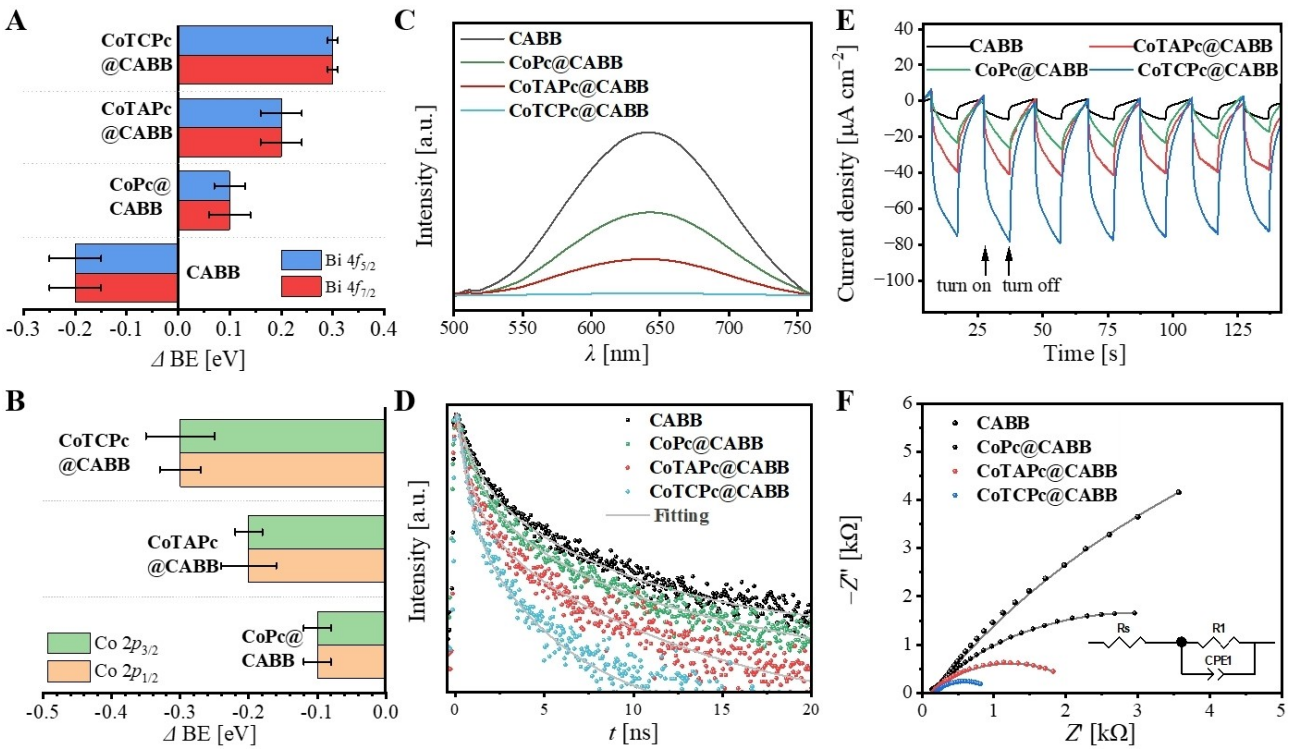

Figure 3. Light-induced shifts (*Δ*BE) in (A) Bi 4*f* and (B) Co 2p binding energy values from ISI-XPS. (C) Steady-state fluorescence spectroscopy, (D) time-resolved fluorescence spectroscopy, (E) non-biased photocurrent response and (F) EIS results of **CABB** (black), **CoPc@CABB** (green), **CoTAPc@CABB** (red) and **CoTCPc@CABB** (blue). Error bars are the standard deviations from two repetitive measurements.

tial differences in the light-induced shifts in both Bi and Co binding energy values between **CoTCPc@CABB** and **CABB** should benefit from the directional electron transfer via the presumable C–O–Bi linking model as proposed in Figure 2F.

Additionally, a sequence of control experiments was operated to evaluate the interfacial charge transfer between the molecular catalysts and the **CABB** surface. Firstly, the electron consumption kinetics were determined by both steady and time-resolved fluorescence spectroscopies in a solid state. The steady fluorescent spectrum of **CABB** in Figure 3C reveals a structureless emission band at 645 nm upon excitation at 365 nm, which was efficiently quenched by the immobilization of cobalt catalysts with an increasing extent from **CoPc** to **CoTAPc** then to **CoTCPc**. For **CoTCPc@CABB**, the quenching efficiency ($\eta_{quenching}$) reaches 99 %, far exceeding that of **CoTAPc@CABB** (67 %) and **CoPc@CABB** (50 %). This is presumably thanks to the efficient electron extraction from **CABB** to **CoTCPc** via Bi–O bond, consistent with ISI-XPS results. Further, we collected the time-resolved fluorescence decays for the above emission band at 645 nm from the **CABB**-based materials. The initial emission life (τ) of bare **CABB** was measured as 7.5 ± 0.3 ns, which was substantially shortened in the presence of **CoPc** (4.4 ± 0.2 ns), **CoTAPc** (2.4 ± 0.1 ns) and **CoTCPc** (1.4 ± 0.1 ns) in an increasing order (Figure 3D and Table S7). Both the quenching studies demonstrate the faster electron consumption by the anchorage of molecular catalysts, and the trend of electron consumption (quenching) efficiency is consistent with that of the strengths of the molecule-**CABB** electronic interactions as observed by XPS (Table S4). In addition, under visible light irradiation, the non-biased photocurrents of these molecular hybrid photocatalysts deposited on FTO slides are all higher than the **CABB**-only sample (Figure 3E). In particular, the photocurrent values display a decreasing sequence of **CoTCPc@CABB**, **CoTAPc@CABB**, **CoPc@CABB** and **CABB**. Accordingly, the electrochemical impedance spectroscopy (EIS; Figure 3F) under light irradiation also reveals the smallest charge-transfer resistance (see Table S8 for values) of **CoTCPc@CABB** among the **CABB**-based photocatalysts. The above photocurrent and EIS measurements further indicate the much-expedited charge separation kinetics by grafting the cobalt catalysts, and **CoTCPc** with the carboxyl anchors being the most significant one. Ultimately, the above comparative experiments clearly demonstrate that the carboxyl anchors of **CoTCPc** bound at the Bi atoms of the **CABB** surfaces allow the optimal, directional electron delivery for promising photocatalytic performance.

Visible-Light-Driven CO_2 Reduction

Finally, the performances of the **CABB**-based photocatalysts for CO_2 reduction were measured in a gas-solid system (Figure S19) containing 1 atm CO_2 and water vapor, without any organic sacrificial agent, irradiated by visible light (100 mW/cm^2, ≥ 400 nm). The gas chromatographic analyses

show that the main gas products are CO and O_2, with negligible CH_4 and H_2 (Figures 4A, 4B and S20), representing the first example of Pb-free-MHP-based molecular hybrid photocatalysts for CO_2 reduction with water as the electron source. The origins of products were identified by $^{13}CO_2$ and $H_2{}^{18}O$ isotope labeling experiments (Figure 4C). In detail, the mass spectra clearly show the gas signals with the *m*/*z* peaks at 29 and 36, which can be assigned to ^{13}CO and $^{18}O_2$, respectively, clearly indicating that CO comes from CO_2 reduction and O_2 originates from water oxidation rather than the decomposition of organic components. It was also noticed that CO and O_2 could not be detected with no photocatalyst, CO_2, or light, meaning that each of these components is indispensable for effective photocatalysis (Figure 4D).

The pristine **CABB** displays a modest CO generation rate of $18\pm4\ \mu mol\,g^{-1}h^{-1}$ (Figure 4A and 4B). In contrast, the immobilization of each cobalt catalyst on the **CABB** surface can substantially accelerate the CO_2 photoreduction to CO, suggesting the effective installation of active sites on the **CABB** semiconductor. Among them, **CoTCPc@CABB** achieved the highest CO generation rate of $150\pm6\ \mu mol\,g^{-1}h^{-1}$, which is ca. 8.3, 6.0, 2.1 times higher than those of **CABB** ($18\pm4\ \mu mol\,g^{-1}h^{-1}$), **CoPc@CABB** ($25\pm5\ \mu mol\,g^{-1}h^{-1}$) and **CoTAPc@CABB** ($72\pm6\ \mu mol\,g^{-1}h^{-1}$), respectively. We further optimized the **CoTCPc** loading in synthesis to obtain the best performance, where the CO yields of corresponding **CoTCPc@CABB** samples reveal a volcano trend with the optimal ratio of **CoTCPc**:**CABB** ($m:m$) = 1:10 (Figure 4E). Apparently, the CO yield was increased along with more active sites from the higher catalyst loading, while it decreased with excess **CoTCPc** which may pose inner-filter effects[19] with its strong absorbance to hinder the light absorption of **CABB**.

It can be observed that the yield ratio of CO:O_2 with **CoTCPc@CABB** is approximately 2:1 (150 ± 6 vs. $77\pm6\ \mu mol\,g^{-1}h^{-1}$), consistent with the electron consumption ratio between CO_2-to-CO conversion ($2e^-$) and water oxidation reaction ($4e^-$), suggesting the full utilization of photogenerated electrons and holes as well as the stability of the photocatalyst. While the CO_2 reduction is mediated by the immobilized molecular catalyst, the formation of the O–O bond during water oxidation at the MHP can be proposed to be a water nucleophilic attack mechanism at a formal M=O (M = Bi/Ag in our case) intermediate, as previously reported.[16] The robustness of **CoTCPc@CABB** can be further confirmed by reusing the photocatalyst in four successive cycles (Figure 4F), which corresponds to an excellent overall CO yield of $7340\pm160\ \mu mol\,g^{-1}$ and O_2 yield of $3520\pm120\ \mu mol\,g^{-1}$ within 48 h of photocatalysis. The unchanged PXRD (Figure S21), XPS spectra (Figure S22) and TEM (Figure S23) results of **CoTCPc@CABB** after photocatalysis also demonstrate its remarkable durability. Especially, the Co 2p XPS spectrum of **CoTCPc@CABB** after catalysis did not show the emergence of Co(0) or Co-based oxides, suggesting the unaltered molecular nature of the immobilized Co catalyst.

Compared to previous MHP-based molecular hybrid photocatalysts for CO_2 reduction,[10–11] **CoTCPc@CABB** system exhibits comparable activity, selectivity and stability

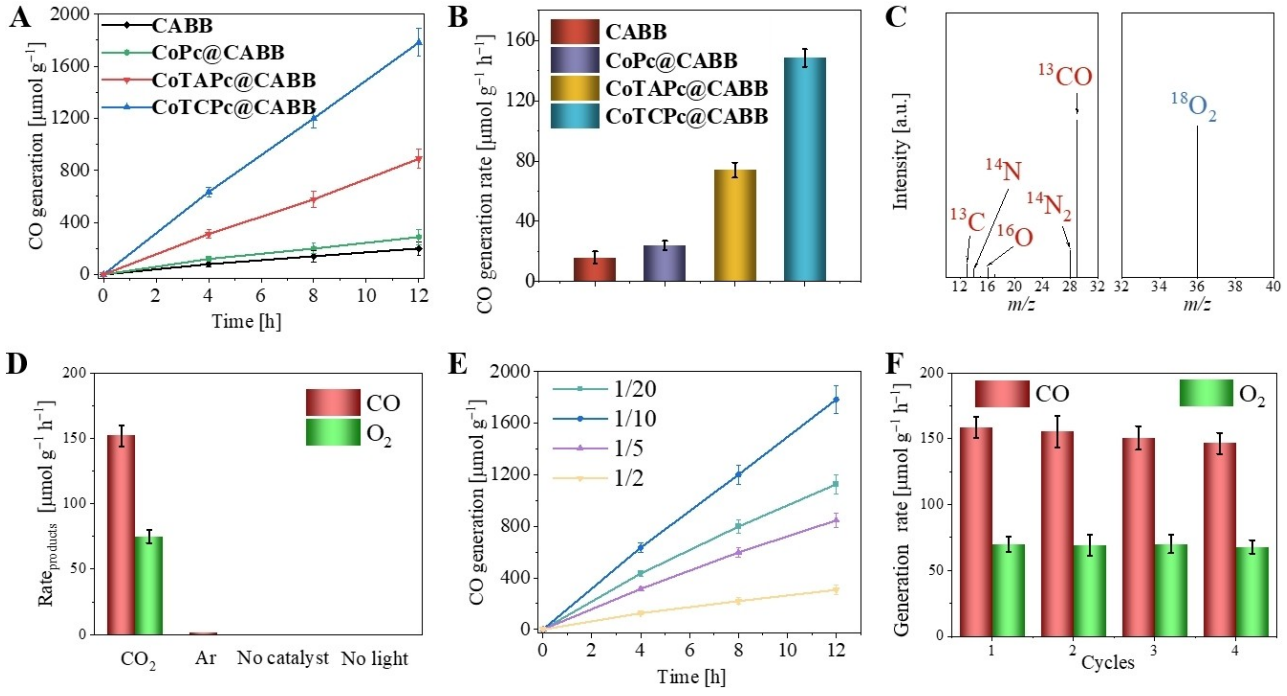

Figure 4. (A) CO yields and (B) CO generation rates of **CABB** (black), **CoPc@CABB** (green), **CoTAPc@CABB** (red) and **CoTCPc@CABB** (blue) in photocatalytic CO_2 reduction. (C) The $^{13}CO_2$ and $H_2{}^{18}O$ isotope labeling experiment by using **CoTCPc@CABB**. (D) CO and O_2 yields in control experiments. (E) CO yields of photocatalytic CO_2 reduction products of **CoTCPc@CABB** with different **CoTCPc/CABB** mass ratios in synthesis. (F) **CoTCPc@CABB** in four successive cycles of 12-h photocatalysis. Error bars are the standard deviations from three parallel measurements.

while avoiding the use of toxic Pb element, highly scarce metals, organic solvent and organic sacrificial reagent, suggesting its potential applications in a much more sustainable manner. More importantly, the remarkable CO generation rate of $150 \pm 6\ \mu mol\ g^{-1} h^{-1}$ from the optimal **CoTCPc@CABB** system corresponds to a record-high electron consumption rate of $300 \pm 13\ \mu mol\ g^{-1} h^{-1}$ among the documented MHP-based photocatalysts for CO_2 reduction coupled with water oxidation ($< 150\ \mu mol\ g^{-1} h^{-1}$; Table S9). These comparisons clearly demonstrate a significant advance in the development of MHP-based photocatalysts for artificial photosynthesis.

Based on the above discussion, the excellent performance by **CoTCPc@CABB** for CO_2 photoreduction to CO can be attributed to its carboxyl anchors, which firstly pose electron-withdrawing effects on the catalyst to afford lower catalytic overpotential. More importantly, the optimal matching between **CoTCPc** and **CABB**, which is via the carboxyl anchorage at the Bi atoms that directly provide photogenerated electrons, greatly accelerates the interfacial electron transfer kinetics, ultimately accomplishing the impressive photocatalytic performance. On the other hand, although **CoTAPc** demands a more negative potential for CO_2 reduction than **CoPc** from comparative CV curves (Figure S6), its **CABB**-based photocatalyst still outperforms **CoPc@CABB** even with a lower catalyst loading (3.0 vs 4.0 w%; Table S2). This contradiction infers that the additional interactions between the molecular catalyst and the MHP surface via the anchors (indicated by XPS and ISI-XPS shifts, Tables S4 and S6) should play a more important role than the intrinsic activity of the catalyst in the photocatalysis. All the above results highlight the versatile strategies for anchoring molecular catalysts on the MHP-based photocatalysts in boosting their catalytic performances.

Conclusion

In summary, we here present the first example of Pb-free-MHP-based molecular hybrid photocatalysts for CO_2 reduction coupled with stoichiometric water oxidation to oxygen. The optimal **CoTCPc@CABB** photocatalyst achieves the record-high electron consumption rate of $300 \pm 13\ \mu mol\ g^{-1} h^{-1}$ compared to other MHP systems ($< 150\ \mu mol\ g^{-1} h^{-1}$) reported so far. Multiple ex situ or in situ spectroscopic experiments combined with computational studies have been deliberately designed to demonstrate the presence and functions of strong interfacial interactions and good electronic matching between molecular catalysts and the MHP surfaces. More importantly, besides the promotive electronic effects, the above results have confirmed that the carboxyl anchors of **CoTCPc** can pinpoint the Bi atoms of **CABB** to construct the optimal pathways for directional transfer of the photogenerated electrons to the **CoTCPc** catalyst, which substantially accelerates the interfacial electron transfer kinetics, eventually achieving the high efficiency in artificial photosynthesis. Overall, we believe that this work will pave a new avenue for the subtle design of high-performance MHP-based molecular hybrid photocatalysts for sustainable CO_2 photoreduction, as well as provide valuable mechanistic insights and experimental orientations in examining the molecule-MHP interfaces.

Author Contributions

T. B. L., M. Z., J. W. W. and Y. F. M. conceived this project, organized the collaborations and supervised the progress, J. S. Z. operated most synthesis, characterization and photocatalytic experiments of MHP-based materials, Z. M. L. and J. W. W. synthesized the metal complexes, Z. M. L. ran the homogeneous electrochemistry, L. V., M. S. and D. M. collected and simulated the XAS data, J. S. Z., J. W. W. and Y. F. M. analyzed the bulk data, J. W. W., M. Z. and T. B. L. provided the funding. J. S. Z., J. W. W., L. Y. W., M. Z. and T. B. L. co-wrote the main draft of the manuscript. The manuscript was written through contributions of all authors. All authors have given approval to the final version of the manuscript.

Acknowledgments

This work was financially supported by the National Key R&D Program of China (2022YFA1502902) and the Natural Science Foundation of China (22305214). Dooshaye Moonshiram acknowledges supports the Spanish Ministerio de Ciencia, Innovacion y Universidades grant (PID2019-111086RA-I00), oriented project to the ecological transition and the digital transition (TED2021-132757B-I00), PIE grant from CSIC-ICMM (20226AT001) and the Ramon y Cajal Fellowship (RYC2020-029863-I). Yan-Fei Mu acknowledges the Jiangsu Funding Program for Excellent Postdoctoral Talent (2022ZB616).

Conflict of Interest

The authors declare no conflict of interest.

Data Availability Statement

The data that support the findings of this study are available from the corresponding author upon reasonable request.

Keywords: lead-free halide perovskite · directed electron transfer · CO_2 reduction · molecular hybrid photocatalyst · cobalt phthalocyanine

[1] J. W. Wang, F. Ma, T. Jin, P. He, Z. M. Luo, S. Kupfer, M. Karnahl, F. Zhao, Z. Xu, T. Jin, T. Lian, Y. L. Huang, L. Jiang, L. Z. Fu, G. Ouyang, X. Y. Yi, *J. Am. Chem. Soc.* **2023**, *145*, 676–688.

[2] K. E. Dalle, J. Warnan, J. J. Leung, B. Reuillard, I. S. Karmel, E. Reisner, *Chem. Rev.* **2019**, *119*, 2752–2875.
[3] J. W. Wang, L. Jiang, H. H. Huang, Z. Han, G. Ouyang, *Nat. Commun.* **2021**, *12*, 4276.
[4] F. Ma, Z.-M. Luo, J.-W. Wang, B. M. Aramburu-Trošelj, G. Ouyang, *Coord. Chem. Rev.* **2024**, *500*, 215529.
[5] *Nat. Catal.* **2019**, *2*, 735–735.
[6] J. Wang, Y. Shi, Y. Wang, Z. Li, *ACS Energy Lett.* **2022**, *7*, 2043–2059.
[7] W. Song, G. Qi, B. Liu, *J. Mater. Chem. A* **2023**, *11*, 12482–12498.
[8] J. San Martin, N. Dang, E. Raulerson, M. C. Beard, J. Hartenberger, Y. Yan, *Angew. Chem. Int. Ed.* **2022**, *61*, e202205572.
[9] Y.-F. Mu, J.-S. Zhao, L.-Y. Wu, K.-Y. Tao, Z.-L. Liu, F.-Q. Bai, D.-C. Zhong, M. Zhang, T.-B. Lu, *Appl. Catal. B-Environ* **2023**, *338*, 123024.
[10] Z.-C. Kong, H.-H. Zhang, J.-F. Liao, Y.-J. Dong, Y. Jiang, H.-Y. Chen, D.-B. Kuang, *Solar RRL* **2019**, *4*, 1900365.
[11] Z. Chen, Y. Hu, J. Wang, Q. Shen, Y. Zhang, C. Ding, Y. Bai, G. Jiang, Z. Li, N. Gaponik, *Chem. Mater.* **2020**, *32*, 1517–1525.
[12] L. Y. Wu, Y. F. Mu, X. X. Guo, W. Zhang, Z. M. Zhang, M. Zhang, T. B. Lu, *Angew. Chem. Int. Ed.* **2019**, *58*, 9491–9495.
[13] Y. F. Mu, W. Zhang, X. X. Guo, G. X. Dong, M. Zhang, T. B. Lu, *ChemSusChem* **2019**, *12*, 4769–4774.
[14] Y. Jiang, J.-F. Liao, H.-Y. Chen, H.-H. Zhang, J.-Y. Li, X.-D. Wang, D.-B. Kuang, *Chem* **2020**, *6*, 766–780.
[15] S. S. Bhosale, A. K. Kharade, E. Jokar, A. Fathi, S. M. Chang, E. W. Diau, *J. Am. Chem. Soc.* **2019**, *141*, 20434–20442.
[16] Y.-F. Mu, H.-L. Liu, M.-R. Zhang, H.-J. Wang, M. Zhang, T.-B. Lu, *J. Energy Chem.* **2023**, *77*, 317–325.
[17] J. T. DuBose, P. V. Kamat, *ACS Energy Lett.* **2022**, *7*, 1994–2011.
[18] X. Chang, T. Wang, P. Yang, G. Zhang, J. Gong, *Adv. Mater.* **2019**, *31*, 1804710.
[19] J.-W. Wang, X. Zhang, L. Velasco, M. Karnahl, Z. Li, Z.-M. Luo, Y. Huang, J. Yu, W. Hu, X. Zhang, K. Yamauchi, K. Sakai, D. Moonshiram, G. Ouyang, *JACS Au* **2023**, *3*, 1984–1997.
[20] J.-W. Wang, D.-C. Zhong, T.-B. Lu, *Coord. Chem. Rev.* **2018**, *377*, 225–236.
[21] W. Zhang, H. H. Huang, Z. M. Luo, F. Ma, S. Gonell, Z. Ke, L. Tan, J. W. Wang, *ChemSusChem* **2024**, DOI: 10.1002/cssc.202301113, e202301113.
[22] D. Liu, M. Zhang, H.-H. Huang, Q. Feng, C. Su, A. Mo, J.-W. Wang, Z. Qi, X. Zhang, L. Jiang, Z. Chen, *ACS Sustainable Chem. Eng.* **2021**, *9*, 9273–9281.
[23] D. C. Liu, H. J. Wang, J. W. Wang, D. C. Zhong, L. Jiang, T. B. Lu, *Chem. Commun.* **2018**, *54*, 11308–11311.
[24] Y. Huang, H. Dai, D. Moonshiram, Z. Li, Z.-M. Luo, J.-H. Zhang, W. Yang, Y. Shen, J.-W. Wang, G. Ouyang, *J. Mater. Chem. A* **2023**, *11*, 2969–2978.
[25] J. W. Wang, H. H. Huang, P. Wang, G. Yang, S. Kupfer, Y. Huang, Z. Li, Z. Ke, G. Ouyang, *JACS Au* **2022**, *2*, 1359–1374.
[26] J. W. Wang, Z. Li, Z. M. Luo, Y. Huang, F. Ma, S. Kupfer, G. Ouyang, *Proc. Natl. Acad. Sci. USA* **2023**, *120*, e2221219120.
[27] J.-W. Wang, M. Gil-Sepulcre, H.-H. Huang, E. Solano, Y.-F. Mu, A. Llobet, G. Ouyang, *Cell Rep. Phys. Sci.* **2021**, *2*, 100681.
[28] A. H. Slavney, T. Hu, A. M. Lindenberg, H. I. Karunadasa, *J. Am. Chem. Soc.* **2016**, *138*, 2138–2141.
[29] M. Pantaler, K. T. Cho, V. I. E. Queloz, I. García Benito, C. Fettkenhauer, I. Anusca, M. K. Nazeeruddin, D. C. Lupascu, G. Grancini, *ACS Energy Lett.* **2018**, *3*, 1781–1786.
[30] J. W. Wang, W. J. Liu, D. C. Zhong, T. B. Lu, *Coord. Chem. Rev.* **2019**, *378*, 237–261.
[31] S. Roy, M. Miller, J. Warnan, J. J. Leung, C. D. Sahm, E. Reisner, *ACS Catal.* **2021**, *11*, 1868–1876.
[32] Z. Li, J.-W. Wang, Y. Huang, G. Ouyang, *Chin. J. Catal.* **2023**, *49*, 160–167.
[33] J. De Roo, M. Ibanez, P. Geiregat, G. Nedelcu, W. Walravens, J. Maes, J. C. Martins, I. Van Driessche, M. V. Kovalenko, Z. Hens, *ACS Nano* **2016**, *10*, 2071–2081.
[34] X. Li, Y. Wang, H. Sun, H. Zeng, *Adv. Mater.* **2017**, *29*, 1701185.
[35] P. J. Han, A. L. Rheingold, W. C. Trogler, *Inorg. Chem.* **2013**, *52*, 12033–12045.
[36] M. Wang, A. Loiudice, V. Okatenko, I. D. Sharp, R. Buonsanti, *Chem. Sci.* **2023**, *14*, 1097–1104.
[37] L. Velasco, C. Liu, X. Zhang, S. Grau, M. Gil-Sepulcre, C. Gimbert-Suriñach, A. Picón, A. Llobet, S. DeBeer, D. Moonshiram, *ChemSusChem* **2023**, *16*, e202300719.
[38] M. Goswami, V. Lyaskovskyy, S. R. Domingos, W. J. Buma, S. Woutersen, O. Troeppner, I. Ivanovic-Burmazovic, H. Lu, X. Cui, X. P. Zhang, E. J. Reijerse, S. DeBeer, M. M. van Schooneveld, F. F. Pfaff, K. Ray, B. de Bruin, *J. Am. Chem. Soc.* **2015**, *137*, 5468–5479.
[39] W. Mao, D. Fehn, F. W. Heinemann, A. Scheurer, M. van Gastel, S. A. V. Jannuzzi, S. DeBeer, D. Munz, K. Meyer, *Angew. Chem. Int. Ed.* **2022**, *61*, e202206848.
[40] T. E. Westre, P. Kennepohl, J. G. DeWitt, B. Hedman, K. O. Hodgson, E. I. Solomon, *J. Am. Chem. Soc.* **1997**, *119*, 6297–6314.
[41] K. E. Loeb, T. E. Westre, T. J. Kappock, N. Mitic, E. Glasfeld, J. P. Caradonna, B. Hedman, K. O. Hodgson, E. I. Solomon, *J. Am. Chem. Soc.* **1997**, *119*, 1901–1915.
[42] S. DeBeer George, P. Brant, E. I. Solomon, *J. Am. Chem. Soc.* **2005**, *127*, 667–674.

Manuscript received: January 19, 2024
Accepted manuscript online: February 29, 2024
Version of record online: ■■, ■■

Research Articles

Photocatalysis

J.-S. Zhao, Y.-F. Mu, L.-Y. Wu, Z.-M. Luo, L. Velasco, M. Sauvan, D. Moonshiram, J.-W. Wang,* M. Zhang,* T.-B. Lu* e202401344

Directed Electron Delivery from a Pb-Free Halide Perovskite to a Co(II) Molecular Catalyst Boosts CO_2 Photoreduction Coupled with Water Oxidation

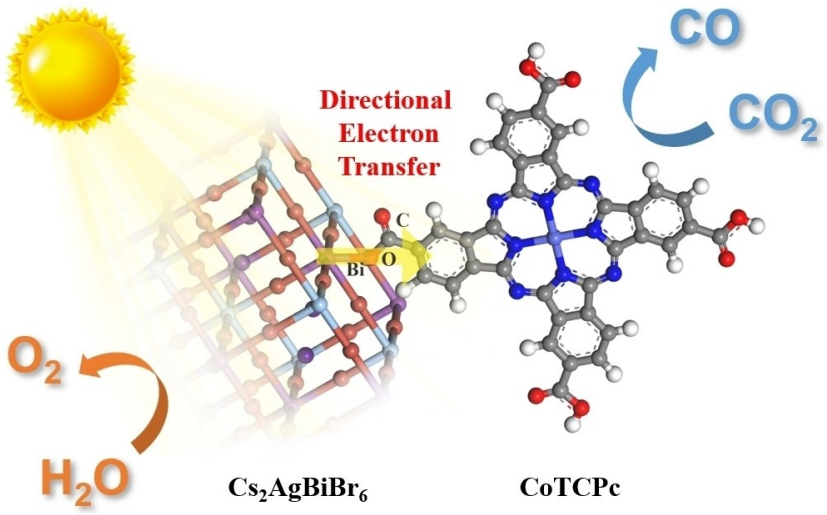

A metal halide photocatalyst immobilized with a molecular catalyst achieves an optimal performance for visible-light-driven CO_2-to-CO conversion coupled with water oxidation to O_2, which mainly benefits from the rapid directional electron transfer from the metal halide to the catalyst via its carboxyl anchors.